

# Decentralized Uncertainty-Aware Active Search with a Team of Aerial Robots

Wennie Tabib, John Stecklein, Caleb McDowell, Kshitij Goel, Felix Jonathan, Abhishek Rathod, Meghan Kokoski, Edsel Burkholder, Brian Wallace, Luis Ernesto Navarro-Serment, Nikhil Angad Bakshi, Tejus Gupta, Norman Papernick, David Guttendorf, Erik E. Kahn, Jessica Kasemer, Jesse Holdaway, and Jeff Schneider

The Robotics Institute, Carnegie Mellon University, Pittsburgh, PA 15213 USA  
 {wtabib, jsteckle, cmcdowel, kgoel1, fjonatha, arathod2, mkokoski, eburkhol, luisn, nabakshi, tejusg, norm, davidg, eekahn, jkasemer, jholdawa, jeff4}@andrew.cmu.edu



Fig. 1: The decentralized, multi-agent team of aerial robots autonomously searches for and localizes objects of interest (OOIs) with approximately 3 m error at altitudes up to 60 m. (top) A team of three aerial systems conducts active search. (bottom-left) Onboard view of OOI (outlined in yellow) detected in real-time. (bottom-right) Location of OOI plotted on shared map generated by the robot team with trajectories plotted as lines. The OOI detection is shown as a yellow dot. A view of the OOI taken on the ground is inset.

**Abstract.** Rapid search and rescue is critical to maximizing survival rates following natural disasters. However, these efforts are challenged by the need to search large disaster zones, lack of reliability in the communications infrastructure, and *a priori* unknown numbers of objects of interest (OOIs), such as injured survivors. Aerial robots are increasingly being deployed for search and rescue due to their

high mobility, but there remains a gap in deploying multi-robot autonomous aerial systems for methodical search of large environments. Prior works have relied on preprogrammed paths from human operators or are evaluated only in simulation. We bridge these gaps in the state of the art by developing and demonstrating a decentralized active search system, which biases its trajectories to take additional views of uncertain OOIs. The methodology leverages stochasticity for rapid coverage in communication denied scenarios. When communications are available, robots share poses, goals, and OOI information to accelerate the rate of search. Detections from multiple images and vehicles are fused to provide a mean and covariance for each OOI location. Extensive simulations and hardware experiments in Bloomington, OH, are conducted to validate the approach. The results demonstrate the active search approach outperforms greedy coverage-based planning in communication-denied scenarios while maintaining comparable performance in communication-enabled scenarios. The results also demonstrate the ability to detect and localize all *a priori* unknown OOIs with a mean error of approximately 3 m at flight altitudes between 50 m to 60 m.

## 1 Supplementary Materials

Videos of the experiments are available at:

- Two robot search with OOIs: <https://youtu.be/qhJS2JhdbAE>;
- Three robot search with Apriltags: <https://youtu.be/xgLnS2IFCQQ>; and
- Two robot search without targets: <https://youtu.be/lzh8MI34enw>.

Open-source software is available at: <https://github.com/rislab/guts-sandbox>.

## 2 Introduction

Rapid emergency response is key to maximizing the survival rate following a disaster. Rescuing a victim within the first 24 hours yields a survival rate of 90%, which drops precipitously to 5-10% after 72 hours [1]. Due to their speed, agility, and maneuverability in challenging three dimensional environments, unmanned aerial systems are increasingly being deployed to facilitate search and rescue [2]. Because the number of victims may be *a priori* unknown, automated methods are needed to systematically and methodically cover the disaster area. An additional challenge arises when communication networks fail, which may occur during severe natural disasters. The problem this work seeks to address is how to autonomously and rapidly search an area to discover objects of interest (OOIs), such as injured persons, while remaining robust to communication dropouts.

There have been several recent works in autonomy for search and environment monitoring that are related to our work. Stache et al. [3] develop an environment monitoring system, which uses a Gaussian Process as a decision function, to modulate an aerial robot’s altitude according to the accuracy of semantic segmentation. The objective is to maximize the classification accuracy of objects in the images. While the work is evaluated in simulation, it is not deployed in real world experiments. In contrast, our active search methodology is demonstrated with a team of up to three aerial robots. Horyna et al. [4] leverage multi-agent flocking behaviors to increase the reliability of OOI detection. When an OOI is detected, one of the agents may separate to confirm the detection. In contrast, the

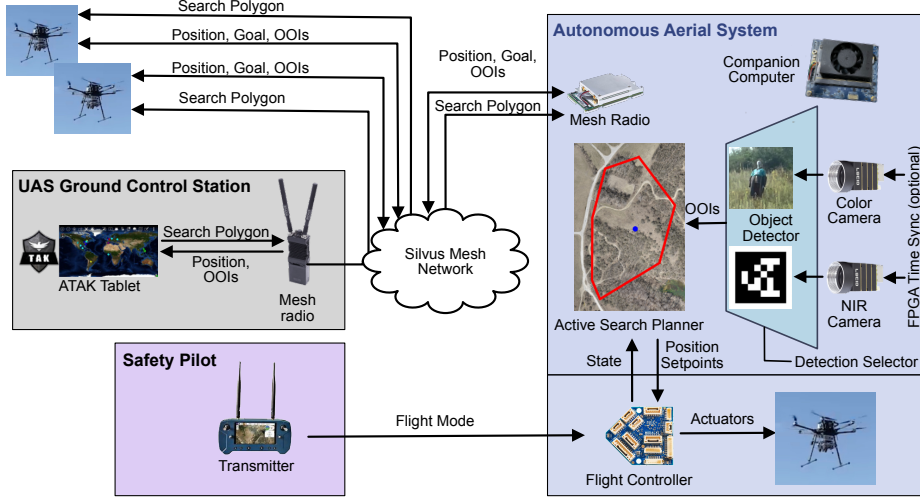


Fig. 2: System diagram for the active search approach. An operator uses the Android Team Awareness Kit (ATAK) app on a tablet to draw a convex polygon of an area for the aerial systems to search. The polygon is sent to one or more robots over a Silvus mesh radio network. Safety pilots launch the vehicles. All search operations are conducted without human intervention. The robot receives state information from the flight controller and camera images are processed to localize OOIs on the ground below. The planner sends position setpoints to the flight controller, which are used to send actuator commands to the motors. When communications are enabled, the robot transmits position, target, and goal information to other robots. When the battery is depleted, the robots return to their takeoff locations and the safety pilots land their vehicles.

loss function in this work enables reflyes over uncertain OOIs while maximizing coverage of the space.

**Contributions:** We extend prior work in active search by Bakshi et al. [5] and provide the following contributions. First, we modify the loss function to incorporate goals from other robots when planning the next best action and provide analysis for a multi-agent aerial team both in simulation and real-world experiments. We also analyze the effects of communication in real-world hardware trials and report the OOI localization accuracy. Finally, we provide an efficient C++ implementation of the active search algorithm with Python bindings for ease of prototyping and deployment to hardware.

### 3 Technical Approach

**Notation** Lowercase boldface symbols represent column vectors (e.g.,  $\mathbf{b}$ ). The  $i$ th entry of a vector  $\mathbf{b}$  is denoted as  $b_i$ . Uppercase bold letters (e.g.,  $\mathbf{B}$ ) represent matrices or sets. Sets and matrices may have the subscript  $\mathbf{B}_{a:b}$ , which means that the matrix or set is composed of data (e.g., row vectors or scalars) from timestamp  $a$  through timestamp  $b$ , inclusive. The transpose of a matrix  $\mathbf{B}$  is denoted as  $\mathbf{B}^\top$ . A square matrix with nonzero entries  $\mathbf{b}$  along the diagonal is represented as  $\text{diag}(\mathbf{b})$ . The  $\ell_2$ -norm of a vector  $\mathbf{b}$  is written as  $\|\mathbf{b}\|_2$ . Where it is important to denote that a particular value is maintained by robot  $j$ , it is written as a superscript (i.e.,  $\mathbf{b}^j$ ).

### 3.1 Active Search

This section details the active search methodology for a single robot (i.e., the communication-denied scenario). It is extended to the communication-enabled case in the next section. Figure 2 provides a system diagram of the approach. Let the environment be represented as a 2D discrete grid with dimension  $M = M_w \times M_h$ , which may be flattened into a vector,  $\beta \in \mathbb{R}^M$ .  $\mathbf{x}_i \in \mathbb{R}^{1 \times M}$  is a one-hot sensing row vector. The aerial system sensing action model consists of all the cells along the straight line between a start and end point. Therefore, an action may be represented using multiple sensing row vectors. Robot positions and OOI detection locations are encoded in  $\mathbf{x}_i$  with 1. All other entries are 0. Each robot also maintains a scalar value  $y_i$ , which represents the output of the object detector as well as the OOI confidence,  $c_i$ .

The data  $\mathbf{D}_{1:i} = \{(\mathbf{x}_1, y_1), \dots, (\mathbf{x}_i, y_i)\}$  consists of all sensor row vectors and observations up to timestep  $i$ . The sensor row vectors are vertically stacked to create a matrix  $\mathbf{X}_{1:i}$  and observations  $y_i$  are also vertically stacked to create a column vector  $\mathbf{y}_{1:i}$ . For example, if  $\mathbf{D}_{1:3} = \{(\mathbf{x}_1, y_1), (\mathbf{x}_2, y_2), (\mathbf{x}_3, y_3)\}$ , then  $\mathbf{X}_{1:3} = [\mathbf{x}_1 \ \mathbf{x}_2 \ \mathbf{x}_3]^\top$  and  $\mathbf{y}_{1:3} = [y_1 \ y_2 \ y_3]^\top$ . Noise is modeled with a diagonal matrix  $\Sigma_{1:i} = \text{diag}([\sigma_1^2 \ \dots \ \sigma_i^2]^\top)$ , where  $\sigma_i^2 = \frac{1}{c_i}$ .

Expectation Maximization is used to estimate the posterior distribution of  $\beta$  given data  $\mathbf{D}_{1:i}$ ,  $p(\beta|\mathbf{D}_{1:i}, \Gamma) = \mathcal{N}(\mu, \mathbf{V})$ , where  $\mu$  and  $\mathbf{V}$  are defined as

$$\begin{aligned} \mathbf{V} &= (\Gamma^{-1} + \mathbf{X}_{1:i}^\top \Sigma_{1:i} \mathbf{X}_{1:i})^{-1} \\ \mu &= \mathbf{V} \mathbf{X}_{1:i}^\top \Sigma_{1:i} \mathbf{y}_{1:i} \end{aligned}$$

and where  $\Gamma \in \text{diag}([\gamma_1 \ \dots \ \gamma_M]^\top)$  are the hidden variables [5, 6]. It should be noted that  $\Gamma \in \mathbb{R}^{M \times M}$  and  $\mu \in \mathbb{R}^M$ .

The Maximization step maximizes the likelihood of  $p(\mathbf{y}_{1:i}|\Gamma, \mathbf{X}_{1:i})$  such that the responsibilities  $\gamma_m$ , where  $m \in [1, \dots, M]$ , may be calculated as:

$$\gamma_m = ([\mathbf{V}]_{mm} + [\mu]_m^2 + 2b_m)/(1 + 2a_m).$$

$a_m = 0.1$  and  $b_m = 1$  in keeping with [5, 6]. After these operations are complete, the robot samples from the posterior  $\tilde{\beta} \sim p(\beta|\mathbf{D}_{1:i})$ .

To select the next sensing action  $\mathbf{X}_{i+1:n} = [\mathbf{x}_{i+1} \ \dots \ \mathbf{x}_n]^\top$ , which lies along a straight line trajectory to a candidate goal location, each agent minimizes the loss function  $\mathcal{L}(\tilde{\beta}, \mathbf{D}_{1:i}, \mathbf{X}_{i+1:n})$

$$\mathcal{L}(\tilde{\beta}, \mathbf{D}_{1:i}, \mathbf{X}_{i+1:n}) = \|\tilde{\beta} - \hat{\beta}\|_2 + \lambda I(\tilde{\beta}, \hat{\beta}) \quad (1)$$

where  $I(\tilde{\beta}, \hat{\beta})$  is an indicator function (defined in Eq. (8)), which encourages the selection of actions that may detect targets outside the most confident set in the sample from the belief,  $\hat{\beta}$ .  $\hat{\beta}$  is calculated as

$$\hat{\beta} = \mathbf{H}_i \mathbf{y}_{1:i} + \mathbf{H}_n \mathbf{X}_{i+1:n} \tilde{\beta} \quad (2)$$

$$[\mathbf{H}_i \ \mathbf{H}_n] = \mathbf{S}([\mathbf{X}_{1:i}^\top \Sigma_{1:i} \ \mathbf{X}_{i+1:n}^\top \Sigma_{i+1:n}]) \quad (3)$$

$$\mathbf{S} = \text{diag}([\mathbf{U}_{k,k}]^{-1}) \quad (4)$$

$$\begin{aligned} \mathbf{U} &= ([\mathbf{X}_{1:i}^\top \Sigma_{1:i} \mathbf{X}_{1:i} + \Gamma^{-1}] \\ &\quad + \mathbf{X}_{i+1:n}^\top \Sigma_{i+1:n} \mathbf{X}_{i+1:n}) \odot \mathbb{I} \end{aligned} \quad (5)$$

$\odot$  denotes elementwise multiplication and  $\mathbb{I}$  represents the identity matrix. In Eq. (4), the notation  $\text{diag}((\mathbf{U}_{k,k})^{-1})$  represents extracting the diagonal entries of the matrix  $\mathbf{U}$ , taking the inverse of these entries, and converting the column vector into a diagonal matrix.

$I(\hat{\boldsymbol{\beta}}, \tilde{\boldsymbol{\beta}})$  is determined by finding half the maximum value of  $\hat{\boldsymbol{\beta}}$  and  $\tilde{\boldsymbol{\beta}}$ , checking if the corresponding value of  $\hat{\beta}_k$  and  $\tilde{\beta}_k$  is larger, respectively, and then rounding to the nearest integer (0 or 1). If all elements of  $\hat{\mathbf{a}}$  match all elements of  $\tilde{\mathbf{a}}$ , then the indicator function specified in Eq. (8) returns a 0 and 1, otherwise.

$$\hat{a}_k = \lfloor \hat{\beta}_k > \max(\hat{\boldsymbol{\beta}})/2 \rfloor \quad (6)$$

$$\tilde{a}_k = \lfloor \tilde{\beta}_k > \max(\tilde{\boldsymbol{\beta}})/2 \rfloor \quad (7)$$

$$I(\tilde{\boldsymbol{\beta}}, \hat{\boldsymbol{\beta}}) = \begin{cases} 0, & \text{if } \hat{a}_k = \tilde{a}_k, \forall k \\ 1, & \text{otherwise} \end{cases} \quad (8)$$

$\lambda = 0.01$  in keeping with [5, 7].

### 3.2 Decentralized Multirobot Planning

This section details how the active search loss function changes when multiple robots share position, goal, and OOI information. Positions, goals, and tracks from other robots are incorporated through updates to the  $\mathbf{X}_{1:i}$  and  $\mathbf{y}_{1:i}$  variables. We will consider what happens to these variables when robot  $j$  receives information from robot  $k$ .

When robot  $j$  receives location information from robot  $k$ , robot  $j$  generates a sensor row vector  $\mathbf{x}_{i+1}^k$  and observation scalar  $y_{i+1}^k$  and appends it to the variables  $\mathbf{X}_{1:i}$  and  $\mathbf{y}_{1:i}$  as in the following equations:

$$\begin{aligned} \mathbf{X}_{1:i+1} &= [\mathbf{x}_1^j \dots \mathbf{x}_i^j \mathbf{x}_{i+1}^k]^\top \\ \mathbf{y}_{1:i+1} &= [y_1^j \dots y_i^j y_{i+1}^k]^\top. \end{aligned}$$

The same update is used when robot  $j$  receives an OOI detection from robot  $k$ . When goals are transmitted, the update is slightly different because there are multiple cells that robot  $k$  traverses. If robot  $j$  has received information that robot  $k$  is at the position encoded in  $\mathbf{x}_{i+1}^k$ , and the next sensing action for robot  $k$  may be specified as  $\mathbf{X}_{i+2:p}^k = [\mathbf{x}_{i+2}^k \dots \mathbf{x}_p^k]^\top$ , then robot  $j$  appends to the variables  $\mathbf{X}_{1:i+1}$  and  $\mathbf{y}_{1:i+1}$  in the following way:

$$\begin{aligned} \mathbf{X}_{1:p} &= [\mathbf{x}_1^j \dots \mathbf{x}_i^j \mathbf{x}_{i+1}^k \mathbf{x}_{i+2}^k \dots \mathbf{x}_p^k]^\top \\ \mathbf{y}_{1:p} &= [y_1^j \dots y_i^j y_{i+1}^k y_{i+2}^k \dots y_p^k]^\top. \end{aligned}$$

$\mathbf{D}_{1:p}^j = (\mathbf{X}_{1:p}, \mathbf{y}_{1:p})$  is used in Eq. (1) in place of  $\mathbf{D}_{1:i}$  since it contains all the information available to robot  $j$ . Formulating  $\mathbf{D}_{1:p}^j$  such that it includes goal information from other robots ensures that robot  $j$  will avoid visiting the same locations.

### 3.3 Trajectory Design and Tracking

Because the hexarotor aerial system used in this work is differentially flat [8], single axis trajectories for  $x$ ,  $y$ ,  $z$  position as well as heading ( $\psi$ ) may be formulated for the robot to track between waypoints. We leverage the single-axis trajectory generation solution of Mueller et al. [9] because it is computationally efficient for size, weight, and power constrained aerial systems. It also enables the time-parameterized calculation of position setpoints, which enables re-planning in flight using all available information up to  $\Delta t$  seconds before reaching the next waypoint. The roots of the derivative of a given polynomial are the times at which the polynomial achieves a critical point, which can be used to ensure the vehicle limits are not exceeded.

### 3.4 Aerial System Hardware Configuration

The aerial system platform is an Inspired Flight 1200 with dimensions  $1.4\text{ m} \times 1.3\text{ m} \times 0.7\text{ m}$  (see Fig. 1). It uses a ModalAI<sup>1</sup> flight controller running a closed-source fork of the ModalAI firmware tag v1.11.3-0.2.3<sup>2</sup>, which is a modified version of the PX4 Autopilot firmware.

Two sensing payloads are developed for the systems. The first sensing payload consists of a global shutter Lucid Vision Phoenix NIR camera, Lucid Vision Phoenix RGB camera, and Teledyne Calibir GX camera. The companion computer is a NVIDIA Jetson AGX Xavier. Silvus Technologies' StreamCaster 4240 mesh radios enable communications between aerial systems and operators via a mobile ad hoc network. The mesh network enables the aerial systems to automatically and dynamically route information between one another and intermediate participating radios (e.g., ground control stations, participating operators, and dedicated relay points).

The second sending payload upgrades the companion computer to a NVIDIA Orin NX with 16 GB RAM and consists of only the RGB camera and Silvus radio.

The NIR camera is used for Apriltag detection experiments and the RGB camera is used for OOI detection. All cameras face at approximately  $45^\circ$  to the ground and communicate with the companion computer via GigE. A tablet running geospatial mapping software called the Android Team Awareness Kit (ATAK) is on the network and transmits zone information to the aerial systems. The aerial systems transmit their poses and object detections to be visualized on the tablet.

### 3.5 Cross-Platform Fusion

During flight, a single OOI may be detected across multiple images and platforms. To accurately localize the OOI, multiple observations of the object are fused into a single estimate, or track. The process of merging the detections into a single track estimate is called cross-platform fusion (CPF). There are two stages to CPF: the first step associates the new detection with currently fused tracks and the second step fuses the tracks. The association step leverages the Euclidean distance from the mean position of the track, which works well when the OOIs are assumed to be stationary. Once the distance cost is calculated, we use the

<sup>1</sup>[https://docs.px4.io/main/en/flight\\_controller/modalai\\_fc\\_v1.html](https://docs.px4.io/main/en/flight_controller/modalai_fc_v1.html)

<sup>2</sup><https://github.com/modalai/px4-firmware/releases/tag/v1.11.3-0.2.3>

Hungarian algorithm [10] to find the best association with both fused and unfused tracks. If the distance exceeds a pre-defined threshold to any known track, a new track is created. Finally, we iterate through the fused tracks to determine whether or not they should be combined with other fused tracks. Once two tracks have been merged, they will stay merged until a greater distance threshold is reached. Fused state is calculated using the inverse covariance intersection [11], which yields a mean and covariance.

## 4 Experiment Design and Results

### 4.1 Simulation Results

The approach is tested in simulation on a Lenovo Thinkpad X1 with an 11th Gen Intel Core i7-1165G7 2.8 GHz CPU, 4 cores (8 hyperthreads), and 16 GB RAM running Ubuntu 20.04. Because the approach is stochastic, multiple trials are run to evaluate the performance. The approach is compared to a deterministic coverage planner that greedily maximizes visiting unknown cells. The results are analyzed by plotting the percent reduction in unknown area as a function of time. For each approach illustrated in Fig. 4 two cases are considered: communication disabled and communication enabled. Our approach, labeled Generalized Uncertainty-Aware Thompson Sampling (GUTS), is shown in blue and the greedy coverage planner is shown in red.

In the communication-denied scenario, GUTS outperforms the coverage-based approach due to the stochasticity. The coverage approach in the communication enabled case (Fig. 4b) slightly outperforms the GUTS approach early on; however, towards the end of the run the GUTS approach slightly outperforms it. For these simulation experiments, no OOIs were included to enable a thorough analysis of the percent coverage achieved by each approach.

Figure 5 provides the same analysis but with one OOI, which is shown as a blue dot. The performance is similar to that shown in Fig. 4. Three robots are used in the simulation and the trajectories for each robot are shown in magenta, yellow, and cyan in Figs. 5c and 5d. The behavior of the GUTS approach is to first explore the environment without stopping even if it finds an uncertain target. When the environment is completely covered, it will re-fly over areas to obtain better views of the targets. This is demonstrated with qualitative simulation results in Fig. 6.

To evaluate the effect of target uncertainty, we vary the value of  $c$  and quantify the number of times the robot views the target(s).  $c$  is the only parameter varied in the simulations shown in Fig. 6. When there is high certainty, the robot executes more exploratory behavior as shown in Figs. 6a and 6d. The 38 and 73 views, respectively, indicate the number of times the robots views the target(s). As the certainty is decreased, the number of views increases.

### 4.2 Hardware Results

To validate the simulations from Section 4.1, the algorithms are deployed to hardware using the aerial vehicles described in Section 3.4. Four analyses are conducted to validate the simulations. All hardware tests were conducted in Bloomington, OH, a 1500+ acre site. An aerial view of the areas flown over during testing is shown in Fig. 3b.

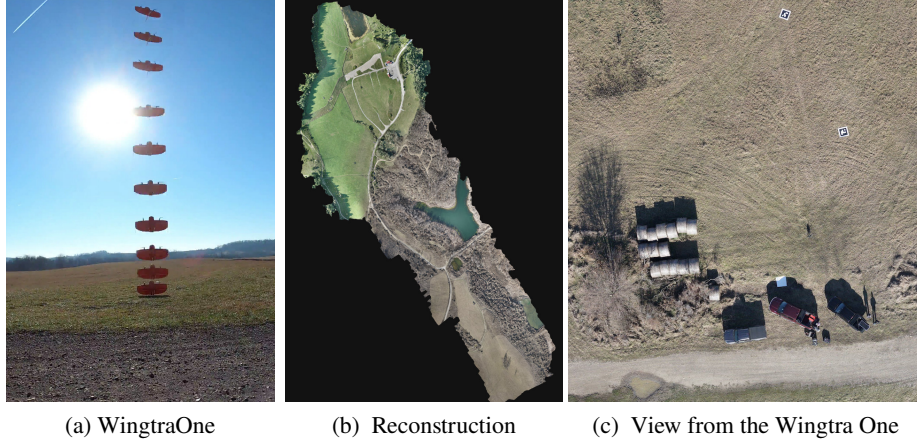


Fig. 3: The (a) WingtraOne<sup>3</sup> VTOL is used to collect images of the test site and produce a (b) high-resolution, geo-registered point cloud and mesh of the environment using the Pix4DMatic<sup>4</sup> photogrammetry software. (c) illustrates a view from the WingtraOne. This image is the test set up for the results shown in Fig. 9.

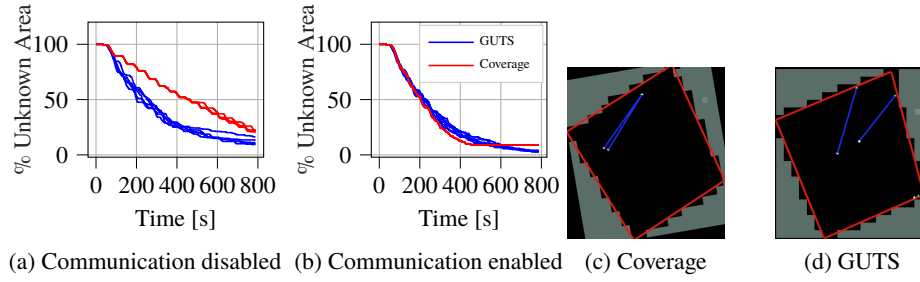


Fig. 4: Simulation results of three robots with and without communication enabled between robots. The results highlight that the stochasticity of the GUTS planner provides better coverage when (a) communication is disabled. (b) The GUTS planner suffers only a slight performance decrease as compared to the coverage planner when communication is enabled. Each approach is run five times for 800 s for a total of 20 trials.

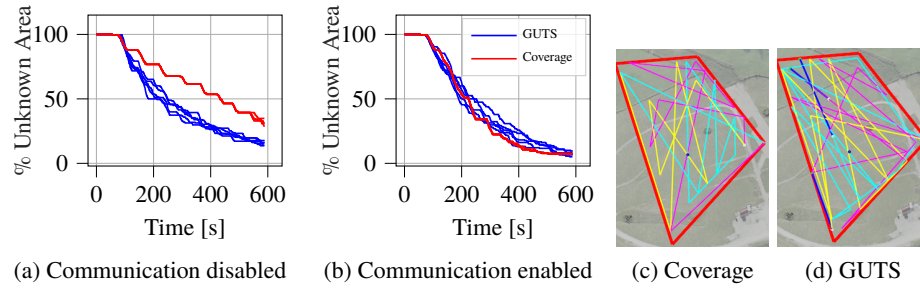


Fig. 5: Simulation results of active search with three robots and one OOI (i.e., blue dot in (c) and (d)). The robot trajectories are shown in magenta, yellow, and cyan in both figures. The blue trajectories are the ones currently being executed in the simulation. Similar to Fig. 4, the GUTS approach outperforms the coverage approach when communications are disabled.



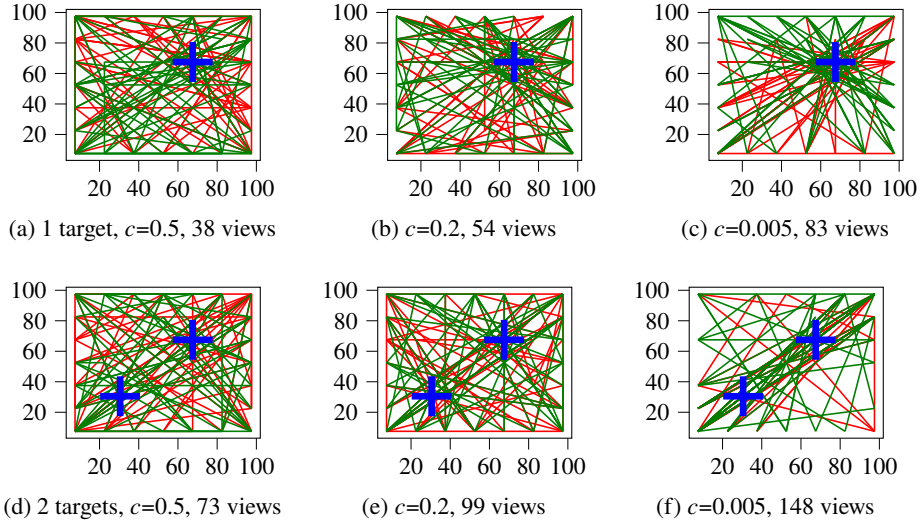


Fig. 6: Simulation results that provide qualitative and quantitative examples of the effect of varying  $c$  for a team of two robots. The OOI locations are shown as blue crosses. The trajectory for robot 1 is shown in red and the trajectory for robot 2 is shown in green. When the confidence is high (e.g., (a) and (d)) the behavior is more exploratory. As the certainty value is decreased (e.g., (b) and (e)), one may see that the action selection is increasingly clustered around the targets. When  $c$  is close to 0.0, the certainty is very low, so the planner will select points that obtain additional views of target (i.e., (c) and (f)). The number of times the robot views the target is counted and provided in the figure caption. The robots will select waypoints to fly over the targets more often as the uncertainty increases.

The cell size used is  $15\text{ m} \times 15\text{ m}$ . The planners plan continuously and the best action is stored. When time runs out, the best action is published. Due to our efficient C++ implementation, 100% of the cells are sampled and evaluated at each planning round.

The first hardware experiment evaluates the performance of the GUTS and coverage planners when communication is disabled with a team of two robots. Figure 7 provides quantitative analysis on hardware that validates the performance of the simulation. In these results, we see that the GUTS planner outperforms the coverage planner when communication is denied. The advantage stems from the stochasticity of the GUTS planner. The areas visited by both robots are shown as transparent cells in Figs. 7b and 7c.

The second hardware experiment evaluates the performance of the GUTS and coverage planners when communication is enabled. A team of two robots searches the areas shown in Figs. 8b and 8c. They share information about poses and goals; however, there are no objects to detect in the environment so no information about tracks is shared. Figure 8a illustrates the coverage as a function of time. We see that when communications between robots are enabled, the coverage approach performs similarly to the GUTS approach, which is in line with what we expect from the simulation results.

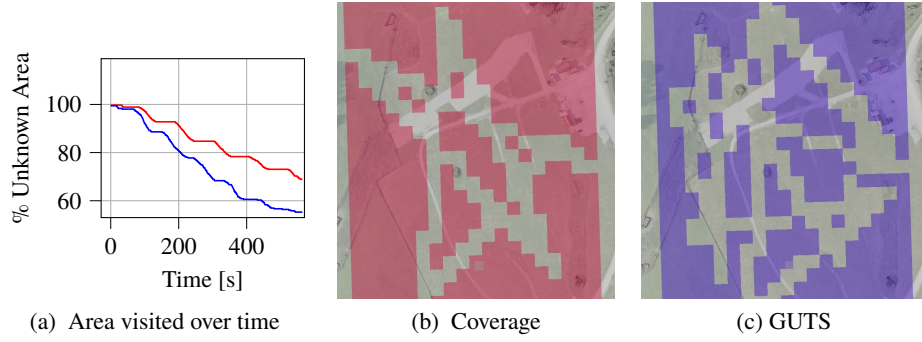


Fig. 7: The number of visited cells as a function of time illustrates the advantage of the decentralized GUTS approach compared to the naive coverage planner. Results obtained from flight data at the test site in Bloomingdale, OH. The flyable area for this experiment is 72 100 m<sup>2</sup>.

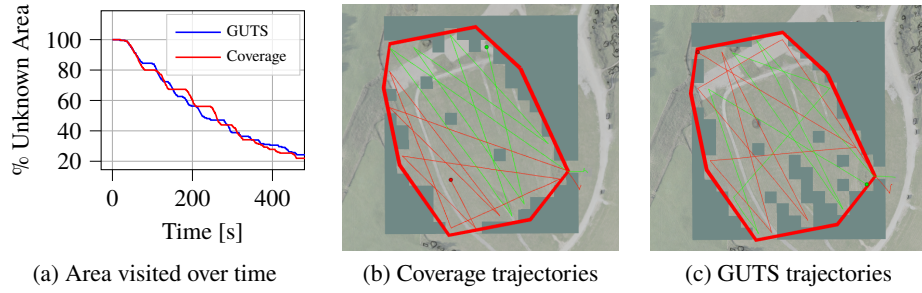


Fig. 8: The effect of enabling communication between two robots is measured in this hardware experiment. The trajectories are shown in red and green. The explored area is shown as transparent cells, which enables the viewer to see the surface terrain. Unknown cells are gray-green and do not enable the viewer to see the terrain below. The GUTS planner performs competitively with the greedy coverage planner. The flyable area for this experiment is 40 700 m<sup>2</sup>.

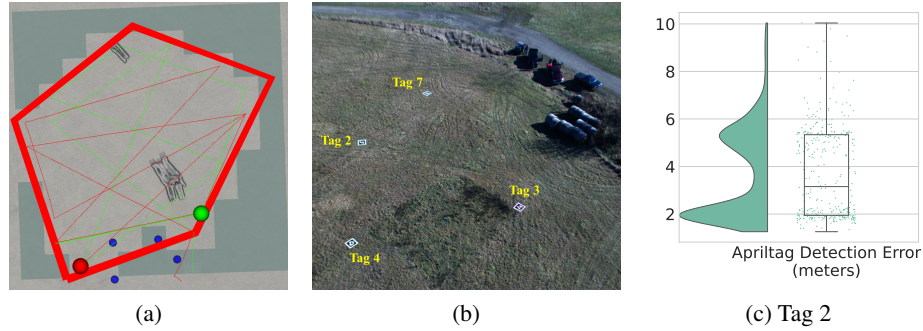


Fig. 9: For this hardware experiment, apriltags are added in the zone and communications are enabled between robots. (b) provides a visualization of the tag positions. Tags 2 and 4 are within the zone outlined in red in (a). The accuracy with which tag 2 is detected is shown in (c). The flyable area for this experiment is 15 000 m<sup>2</sup>.

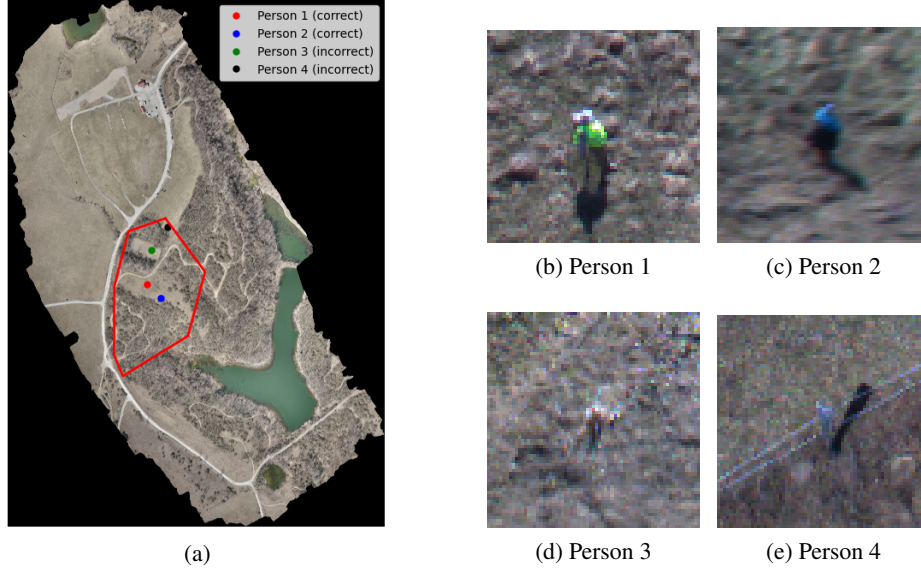


Fig. 10: Four persons were detected within the (a) search zone for this hardware experiment. (b) and (c) are the two correctly detected mannequins hidden in the environment. (d) and (e) are incorrect detections. A video of this experiment may be found at <https://youtu.be/qhJS2JhdbAE>.

The third field test integrates targets and is shown in Fig. 9. Communication is enabled for this trial. These results correspond to the environment shown in Fig. 3c. The targets are shown as blue dots in Fig. 9a and labeled with their IDs in Fig. 9b. Tags 2 and 4 are contained within the boundary of the red zone. Tags 3 and 7 are detected on landing, but are outside the boundary of the red zone and are not included as a result. The raw localization errors (i.e., no CPF) for a representative tag is shown in Fig. 9c. To localize the targets in the global coordinate frame, a ray from the camera is projected to the apriltag and intersected with a plane, which represents the environment. For this test a single trial is conducted with the GUTS planner. The track certainty is fixed to be low ( $c = 0.005$ ). Apriltags are used as targets because they are detected more reliably compared to neural-based object detectors.

The final field test evaluates the effect of incorporating cross-platform fusion (CPF) from Section 3.5 using static mannequins as substitutes for persons in the environment. For all prior experiments, the first sensing payload (Xavier payload) is used, but for this experiment the second sensing payload (Orin NX payload) is used. For this experiment, we use two aerial system to simultaneously cover the search zone illustrated as the red convex polygon in Fig. 10a. Two mannequins are hidden in the environment. No prior knowledge is provided to the system about the number or type of targets in the environment. The CPF system correctly detects both mannequins in the environment (Figs. 10b and 10c) and incorrectly detects two persons (Figs. 10d and 10e). The localization accuracy for person 1 is 2.9 m and 3.6 m for person 2. The flyable area for this red zone was 55 500 m<sup>2</sup>. The detector uses a fine-tuned YOLOv5<sup>5</sup> model.

<sup>5</sup><https://github.com/ultralytics/yolov5>

## 5 Conclusion and Future Work

This paper detailed a system and methodology for decentralized multi-robot active search and analyzed the performance while varying the availability of communications and target uncertainty. A limitation of the current approach is that it is difficult to scale with large numbers of robots and environment extents due to the formulation of the loss function. One way to address this limitation is to leverage information-theoretic grid compression strategies that provide a reduced representation while retaining relevant information. A potential future area of research is to extend the implementation from 2D to 3D as well as consider terrain features where objects may be more likely to exist. Robot assisted search holds the promise of safeguarding lives. To this end, we hope the results presented in this paper as well as open source software release accelerate innovation in this area and benefit the robotics community.

## 6 Acknowledgments

This work was supported in part by the U.S. Army Research Office and the U.S. Army Futures Command under Contract No. W519TC-23-C-0031.

## References

- [1] A. Hakami, A. Kumar, S. J. Shim, and Y. A. Nahleh, "Application of soft systems methodology in solving disaster emergency logistics problems," *International Journal of Industrial and Manufacturing Engineering*, vol. 7, no. 12, pp. 2470–2477, 2013.
- [2] R. Ashour, S. Aldhaheri, and Y. Abu-Kheil, *Applications of UAVs in Search and Rescue*. Cham: Springer International Publishing, 2023, pp. 169–200. [Online]. Available: [https://doi.org/10.1007/978-3-031-32037-8\\_5](https://doi.org/10.1007/978-3-031-32037-8_5)
- [3] F. Stache, J. Westheider, F. Magistri, C. Stachniss, and M. Popović, "Adaptive path planning for uavs for multi-resolution semantic segmentation," *Robotics and Autonomous Systems*, vol. 159, p. 104288, 2023.
- [4] J. Horyna, T. Baca, V. Walter, D. Albani, D. Hert, E. Ferrante, and M. Saska, "Decentralized swarms of unmanned aerial vehicles for search and rescue operations without explicit communication," *Autonomous Robots*, vol. 47, no. 1, pp. 77–93, 2023.
- [5] N. A. Bakshi, T. Gupta, R. Ghods, and J. Schneider, "Guts: Generalized uncertainty-aware thompson sampling for multi-agent active search," in *2023 IEEE International Conference on Robotics and Automation (ICRA)*, 2023, pp. 7735–7741.
- [6] R. Ghods, W. J. Durkin, and J. Schneider, "Multi-Agent Active Search using Realistic Depth-Aware Noise Model," Mar. 2021, arXiv:2011.04825 [cs, eess]. [Online]. Available: <http://arxiv.org/abs/2011.04825>
- [7] N. A. Bakshi and J. Schneider, "Stealthy Terrain-Aware Multi-Agent Active Search," Oct. 2023, arXiv:2310.10961 [cs]. [Online]. Available: <http://arxiv.org/abs/2310.10961>
- [8] D. Mellinger and V. Kumar, "Minimum snap trajectory generation and control for quadrotors," in *2011 IEEE International Conference on Robotics and Automation*, 2011, pp. 2520–2525.
- [9] M. W. Mueller, M. Hehn, and R. D'Andrea, "A computationally efficient motion primitive for quadcopter trajectory generation," *IEEE Transactions on Robotics*, vol. 31, no. 6, pp. 1294–1310, 2015.
- [10] H. W. Kuhn, "The hungarian method for the assignment problem," *Naval research logistics quarterly*, vol. 2, no. 1-2, pp. 83–97, 1955.
- [11] B. Noack, J. Sijs, and U. D. Hanebeck, "Inverse covariance intersection: New insights and properties," in *2017 20th International Conference on Information Fusion (Fusion)*, 2017, pp. 1–8.